VOLCΛNICA

Tracking secondary lahar flow paths and characterizing pulses and surges using infrasound array networks at Volcán de Fuego, Guatemala

Ashley R. Bosa[*α], Jeffrey B. Johnson[α], Silvio De Angelis[β], John J. Lyons[γ], Amilcar Roca[δ], Jacob F. Anderson[α], Amando Pineda[ε]

[α]*Boise State University, Department of Geosciences, Boise, ID, USA.*
[β]*University of Liverpool, Liverpool, UK.*
[γ]*U.S. Geological Survey, Alaska Volcano Observatory, Anchorage, AK, USA.*
[δ]*Instituto Nacional de Sismologia, Vulcanologia, Meteorologia e Hidrologia (INSIVUMEH), Guatemala City, Guatemala.*
[ε]*Independent, Guatemala City, Guatemala.*

Abstract

Lahars are one of the greatest hazards at many volcanoes, including Volcán de Fuego (Guatemala). On 1 December 2018 at 8:00 pm local Guatemala time (~2:06:00 UTC), an hour-long lahar event was detected at Volcán de Fuego by two permanent seismo-acoustic stations along the Las Lajas drainage on the southeast side. To establish the timing, duration, and speed of the lahar, infrasound array records were examined to identify both the source direction(s) and the correlated energy fluctuations at the two stations. Co-located seismic and acoustic signals were also examined, which indicated at least five distinct energy pulses within the lahar record. We infer that varying sediment load and/or changes in flow speed is shown by clear fluctuations in the acoustic and seismic power recorded at one of the stations. This particular event studied with infrasound provides insight into how lahars occur around Volcán de Fuego.

Keywords: Lahar; Infrasound; Seismic; Fuego volcano; Flow evolution

1 INTRODUCTION

Lahar is an Indonesian term to describe mobilized pyroclastic mudflows on or near a volcano. This geohazard can transform between a high sediment "debris flow" lahar (>60 % sediment by volume) and a more dilute "hyperconcentrated flow" (sediment concentration between 20 and 60 % by volume) [Beverage and Culbertson 1964; Pierson 1985; Pierson and Costa 1987], affecting the rheological properties of the mixture. Lahar rheology (as either debris flows or hyperconcentrated flows) are Non-Newtonian [Pierson 1985; Pierson and Costa 1987; Parfitt and Wilson 2009]; when mobilized, they have low viscosities [e.g. 29–93 Pa s at Mangatoetoenui, NZ and 20–320 Pa s at Pine Creek, Mount St. Helens, USA Phillips and Davies 1991; Manville et al. 1998] and speeds up to tens of meters per second [Parfitt and Wilson 2009; Allstadt et al. 2018]. The nature of the flow depends on the velocity, discharge, channel morphology, sediment concentration, and grain-size distribution and segregation [Pierson 1985; Lavigne and Thouret 2003; Dumaisnil et al. 2010; Iverson et al. 2010; Thouret et al. 2020]. As a lahar moves downstream, its rheology and appearance can change as it undergoes bulking and debulk-

ing processes. These flows also exhibit characteristics that produce pulses or surges [Pierson 1985; Thouret et al. 2020] broken down into segments which represent variations in entrainment, dilution, deposition, and flow rheology (Figure 1). In other words, rheology and appearance within a single pulse is transformative and intricate. Many of these characteristics are controlled by factors such as slope, porosity fluctuation, fluid pressures, and variability in flow-path topography [Lavigne and Thouret 2000; Iverson et al. 2010; Thouret et al. 2020].

Although triggering mechanisms are complex, lahars generally occur when abundant, unconsolidated tephra deposits mix with enough water to create a sediment-rich flow on or around the volcano. Lahars can have syn-eruptive, post-eruptive, or a non-eruptive origin [e.g. Pierson et al. 1990; Doyle et al. 2010; Ogiso and Yomogida 2015; Vallance and Iverson 2015; Kataoka et al. 2018]. Major initiation mechanisms include transformations from debris avalanches [e.g. Mount St. Helens, USA: Scott 1988], rapid melting of ice and snow during an eruption [e.g. Nevado del Ruiz, Columbia: Pierson et al. 1990], outbreaks of crater lakes (or other impounded bodies of water) [e.g. Mt. Kelud, Indonesia: Thouret et al. 1998], and rainfall on unconsolidated tephra deposits [e.g. Pierson and Major 2014]. Post-eruptive, "secondary" lahars occur more

frequently and are typically smaller in volume than syn-eruptive, "primary" lahars [Dumaisnil et al. 2010; Pierson and Major 2014; Cando-Jácome and Martínez-Graña 2019; Thouret et al. 2020]. The sporadic behavior, large debris-carrying capacity and potential to travel long distances makes lahars among the most hazardous volcanic phenomena and a significant threat to downstream communities. Mitigation efforts to identify their upstream initiation is essential to providing adequate warnings to those living downstream.

Rainfall accumulation and rainfall intensity appear to be the main driving factors for secondary lahar initiation [Lavigne and Thouret 2000; Capra et al. 2010; Jones et al. 2017; Kataoka et al. 2018]. Many other factors, besides the addition of water, also influence the initiation of a rain-triggered lahar, including: (1) slope instability and channel gradient driven by gravitational forces [e.g. Lavigne and Thouret 2003; Pierson et al. 2013]; (2) the volume and thickness of pyroclastic material and tephra deposits [e.g. Janda et al. 1996; Manville et al. 2000]; (3) the physical characteristics of material being mobilized (i.e. permeability, pore pressure, shear strength of grains, etc.) [e.g. Dumaisnil et al. 2010; Kurokawa et al. 2018]; and (4) presence of vegetation [e.g. Matthews 2002; Lavigne and Thouret 2003; Capra et al. 2010]. However, Jones et al. [2017] note that rainfall on the unconsolidated tephra is the primary trigger of secondary-type lahars.

Lahars, traditionally, have been detected using Acoustic Flow Monitors (AFM), a type of seismic system designed specifically to detect ground vibrations associated with the onset and the physical parameters (i.e. hydrological, morphometric, etc.) of lahars and other gravity-driven mass movements such as debris flows [Arattano and Marchi 2008; Suwa et al. 2011; Kean et al. 2015; Allstadt et al. 2019]. AFMs are typically installed close to expected lahar flow channels and drainages [Hadley and LaHusen 1995; Allstadt et al. 2018]. The close observing distance of AFMs has proven effective in providing timely detections and warnings at several volcanoes, such as Mt. Pinatubo (Philippines), Merapi Volcano (Indonesia), Mt. Ruapehu (New Zealand), and Volcán de Colima (Mexico) [Marcial et al. 1996; Lavigne and Thouret 2000; Cole et al. 2009; Zobin et al. 2009; Sukatja 2016]. Seismic signals during lahars are produced by a variety of sources, including frictional interaction with channel walls, wave-breaking, grain interaction (i.e. particle collision), changes in bedload transport, and splashing due to turbulence [Huang et al. 2007; Cole et al. 2009; Doyle et al. 2011; Walsh et al. 2020]. Generally, seismic monitoring is augmented with other data (i.e. infrasound, rain gauges, cameras, etc.).

The use of infrasound to detect and track lahars is relatively new. Low-frequency acoustic monitoring has been used more extensively in the surveillance of volcanic eruptions, including explosions, eruption intensity [Fee and Matoza 2013; Anderson et al. 2018; John-

son et al. 2018; De Angelis et al. 2019], eruption precursors [Ripepe et al. 2018], and volcanic hazards such as pyroclastic flows (e.g. at Unzen, Japan: Yamasato, 1997; at Soufrière Hills: [Ripepe et al. 2009]). More recently, infrasound has been utilized to detect and track lahars [Johnson and Palma 2015], and other types of non-volcanic debris flows and surficial mass movements [Allstadt et al. 2018; Marchetti et al. 2019]. As a monitoring system, infrasound arrays are a powerful tool that can be used for detecting, tracking, and characterizing flow dynamics of lahars. This study highlights the capabilities of infrasound in detecting and tracking lahars, as well as distinguishing the hydrological and geomorphic pulses and surges that occur within the flow.

1.1 Flow transition in lahars

The abundance of tephra deposits combined with high seasonal rainfall offers favorable conditions for the potential generation of lahars, while the slope, rainfall intensity, and location of the available substrate control the emplacement, magnitude, and propagation of lahars [Swanson and Major 2005; Pierson and Major 2014]. These blankets of volcanic ash greatly reduce the ability of rainfall to infiltrate into the ground, subsequently leading to higher runoff, and increased triggering of lahars [Jones et al. 2017]. Starting as erosive, watery mixtures, lahars typically increase in volume and discharge downstream as they transform into hyperconcentrated flows and sediment-rich debris flows [Beverage and Culbertson 1964; Doyle et al. 2011].

Hyperconcentrated flows are turbulent flows of intermediate mixtures of water and suspended sediment (more concentrated than normal streamflow, but less than debris flows) [Pierson 2005; Doyle et al. 2011]. Debris flows have a much higher particle-volume concentration and are described as viscous fluid flows [Doyle et al. 2011], with a concentrated coarse-grained head, and diluted, liquefied tail [Vallance and Iverson 2015]. Simply stated, transformations between hyperconcentrated flows and debris flows can be described as a change in flow regimes [Scott 1988; Fagents and Baloga 2006], which is dependent on amount, type, and size of sediment [Scott 1988; Fagents and Baloga 2006; Cole et al. 2009; Doyle et al. 2011]. Lahar bulking by erosion and sediment entrainment are thought to control the occurrence of different flow phases [Scott 1988]. Erosion and sediment entrainment takes place by undercutting steep slopes, terrace scarps, and stream banks (i.e. cutbanks around bends) [Vallance and Iverson 2015]. This bulking process causes downstream transformations from water-flood flow, to hyperconcentrated flows, to debris flows [Doyle et al. 2011; Vallance and Iverson 2015], and can transition between sediment concentration depending on erodibility of the channel [Doyle et al. 2011], dilution of the system, and debulking that occurs as the flow interacts with shallower

slopes and perennial streamflow [Scott 1988; Lockwood and Hazlett 2010; Vallance and Iverson 2015]. It is also common for lahars to develop pulses as the flow progresses downstream. Pulses, in this sense, refers to smaller scale regime changes (Figure 1) that progress along the entire observed extent of the channel influenced by larger scale changes in volume, clast size, flux, etc., in response to fluctuations in watershed discharge, rainfall amount, and intensity [Capra et al. 2010; Capra et al. 2018], and bulking/debulking processes that influence fluctuations of erosion and aggradation through space and time [Zanuttigh and Lamberti 2007; Doyle et al. 2010]. Many studies have quantified seismic and infrasonic energy for both lahars and non-volcanic debris flows [e.g. Marcial et al. 1996; Huang et al. 2007; Doyle et al. 2010; Kean et al. 2015]. For example, seismic studies have observed signal correlations with sediment concentration and grain-size distribution in lahars [e.g. Coviello et al. 2018] as well as the fact that increased seismic amplitude and energies correlates to volume concentration increases [Doyle et al. 2010]. However, correlations between sediment transport and material flux and infrasonic signals remain poorly understood.

Volcán de Fuego, with an elevation of 3760 m, is one of the most active stratovolcanoes in Central America; its activity is characterized by frequent Strombolian–Vulcanian type eruptions, lava flows, and persistent degassing [Vallance et al. 2001; Marchetti et al. 2009; Lyons et al. 2010; Lyons and Waite 2011; Naismith et al. 2019]. The volcano is part of the Fuego-Acatenango massif, which trends north–south and includes at least five known eruptive centers [Vallance et al. 2001; Lyons and Waite 2011]. The massif generally erupts high-Al_2O_3 basalt lavas [Lyons and Waite 2011], although compositions such as basaltic-andesites and andesitic lavas have also been reported from prehistoric eruptions [Naismith et al. 2019]. In historical times, Volcán de Fuego has erupted more than 60 times [Vallance et al. 2001; Naismith et al. 2019], with the majority of these events consisting of low-intensity Strombolian eruptions interspersed with discrete violent paroxysms that produced lava flows and pyroclastic density currents (PDC). A sub-Plinian eruption in 1974 produced 0.2 km^3 of tephra [Naismith et al. 2019]; in 1999, the volcano entered a new eruptive period, producing persistent Strombolian eruptions as an open-vent system, interspersed by several, discrete "paroxysmal" eruptions [Lyons et al. 2010; Lyons and Waite 2011; Naismith et al. 2019]. the Instituto Nacional de Sismología, Vulcanología, Meteorología e Hidrología (INSIVUMEH) notes that the volcano has been "erupting vigorously" since 2002 [Global Volcanism Program 2018]. The larger, more violent paroxysms range from volcanic explosivity index (VEI) 2 to VEI 4 [Global Volcanism Program 2013; Naismith et al. 2019], and generally consist of continuous lava flows, explosions sustaining an eruptive plume and gas emission, and po-

tential development of PDCs [Naismith et al. 2019], created either by eruptive column collapse, "boiling over" the crater rim, or lava-dome gravitational collapse [Flynn and Ramsey 2020]. More recently, large eruptions on 13 September 2012 and another on 3 June 2018 produced large PDCs descending the flanks on the south side of the volcano [Naismith et al. 2019]. In 2018, as reported by INSIVUMEH and Coordinadora Nacional para la Reducción de Desastres (CONRED), several pyroclastic flows were registered during the 10-hour paroxysm; the longest PDC runout occurred southeast of the summit, descending the Las Lajas drainage, blanketing the ravine and surrounding landscapes in fresh, hot volcanic ash [Global Volcanism Program 2019; Naismith et al. 2019].

1.2 Volcán de Fuego lahars

Around Volcán de Fuego, secondary lahars are often triggered by heavy rainfall that occurs primarily during afternoon/early evening storms between May and October. Volcán de Fuego's episodic eruptions allow ample unbound pyroclastic material to be deposited on its flanks and in the surrounding river channels. This tephra is easily remobilized by the rain, and as a consequence, lahars can occur dozens of times during a single rainy season [Global Volcanism Program 2013]. Following the 03 June 2018 eruption, INSIVUMEH recorded a total of 33 lahars between 06 and 30 June in various drainages around Volcán de Fuego [Global Volcanism Program 2018]. The frequency of lahars around Volcán de Fuego makes it an ideal field laboratory to observe and analyze these phenomena.

The secondary, rain-triggered lahar event described in this study occurred on 01 December 2018 and lasted approximately 60 minutes. We calculated an average speed of about 6.9 m s^{-1} and identified at least five pulses observed in the acoustic signals. Unfortunately, we were unable to obtain rainfall information prior to the event; however, we infer that a storm was present due to lightning glitches seen in the infrasound signals, as discussed below. Lightning and thunderstorms are common around Volcán de Fuego in the afternoon during the "winter" months (May–October).

2 Data

The Las Lajas channel (Figure 2B) featured in this study is one of many active lahar channels at Volcán de Fuego. Its position was computed using topography from the Shuttle Radar Topography Mission (SRTM) Digital Elevation Map (DEM) with 1 arc-second resolution (~30 × 30 m), acquired from the NASA Earthdata repository on 4 June 2020.
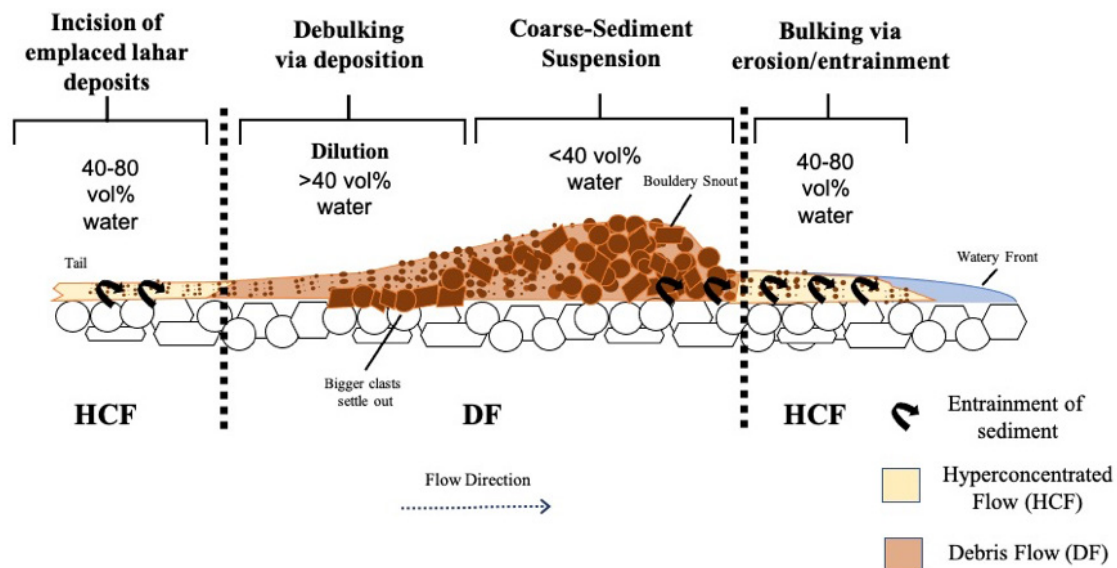
Figure 1: Schematic vertical profiles of lahar flow phases and pulses. Detailed flow properties of each small-scale pulse show a watery front, transitioning into hyperconcentrated flow (HCF) and debris flows (DF) as more sediment is entrained. Towards the tail of a pulse, the flow is more dilute and may transition back to a HCF or muddy streamflow, where free particles have a greater impact on channel walls, increasing erosive power, and entraining more sediment to transform back into a DF lahar. A lahar that has evolved will have multiple pulses that can be detected at different stations as the flow travels downstream.

2.1 Seismic and infrasound network

In this study we use data recorded from a secondary rain-triggered lahar on 1 December 2018 by two permanent, telemetered seismo-acoustic stations located along the Las Lajas drainage; these instruments are part of a larger network installed at Volcán de Fuego to monitor the drainages to the south of the volcano (Figure 2A–B). The network was deployed as a joint effort between INSIVUMEH, the University of Liverpool, and the USGS's Volcanic Disaster Assistance Program (VDAP). This network was designed to monitor both eruptive activity from Volcán de Fuego as well as rapid mass wasting events such as lahars or pyroclastic density currents.

Data in this study come from two arrays, Station FG12 and Station FG13 (operational since July 2018), situated at the edge of the Las Lajas drainage (FG12 is approximately 200 m from main drainage, while FG13 is less than 100 m from the drainage) at slant distances of approximately 6.3 and 9.9 km from the summit of Volcán de Fuego, respectively (Figure 2B). Each station consisted of a broadband seismometer and a three-element infrasound array with ~73 m (FG12) and ~56 m (FG13) aperture (Figure 2C–D). Only two infrasound sensors were operational at the FG13 array at the time of the event analyzed in this study. Lightning damage of cabled sensors is common in the study area and was likely responsible for the failure of one of the sensors.

Infrasound microphones at all stations were Chaparral M60 UHP sensors (with sensitivity of 0.009 V Pa^{-1}) connected to Nanometrics Centaur 24-bit digitizers. The sensor response is flat to within ± 3 dB in the frequency band above 0.03 Hz. Co-located seismic stations were 3-component Nanometrics Trillium Compact Posthole ($T = 120$ s) sensors. Data from all channels were continuously recorded at a sample rate of 50 Hz.

Lahars are common during the winter rainy season (May–October) in the Las Lajas drainage and the analyzed data correspond to an event that occurred at the end of this rainy season. The event on 01 December 2018 was a secondary lahar likely triggered by rainfall as evidenced by thunderstorm activity recorded by the infrasound network [Anderson et al. 2018]. In Figures 3 and 4, the lightning is evident at 00:52:00 UTC–02:08:00 UTC, which largely precedes the lahar event that started around 02:06:00 UTC. Infrasound and seismic signals were filtered above 5 Hz to remove non-lahar signals and noise. Selection of this low corner frequency was based upon previous analysis of debris flows and lahars, which exhibited peak amplitudes at frequencies of 6–8 Hz for seismic and 5 Hz for infrasonic [Cole et al. 2009; Doyle et al. 2010; Johnson and Palma 2015; Lai et al. 2018; Marchetti et al. 2019; Thouret et al. 2020]. In addition, Diaz-Moreno et al. [2020] noted acoustic signals of lahars at Volcán de Fuego with dominant energy in the 1–15 Hz frequency band and Johnson and Palma [2015] found lahar energy is intense above 5 Hz for an event recorded at Volcán Villarrica, Chile. This was also observed in spectral analysis during the identified lahar
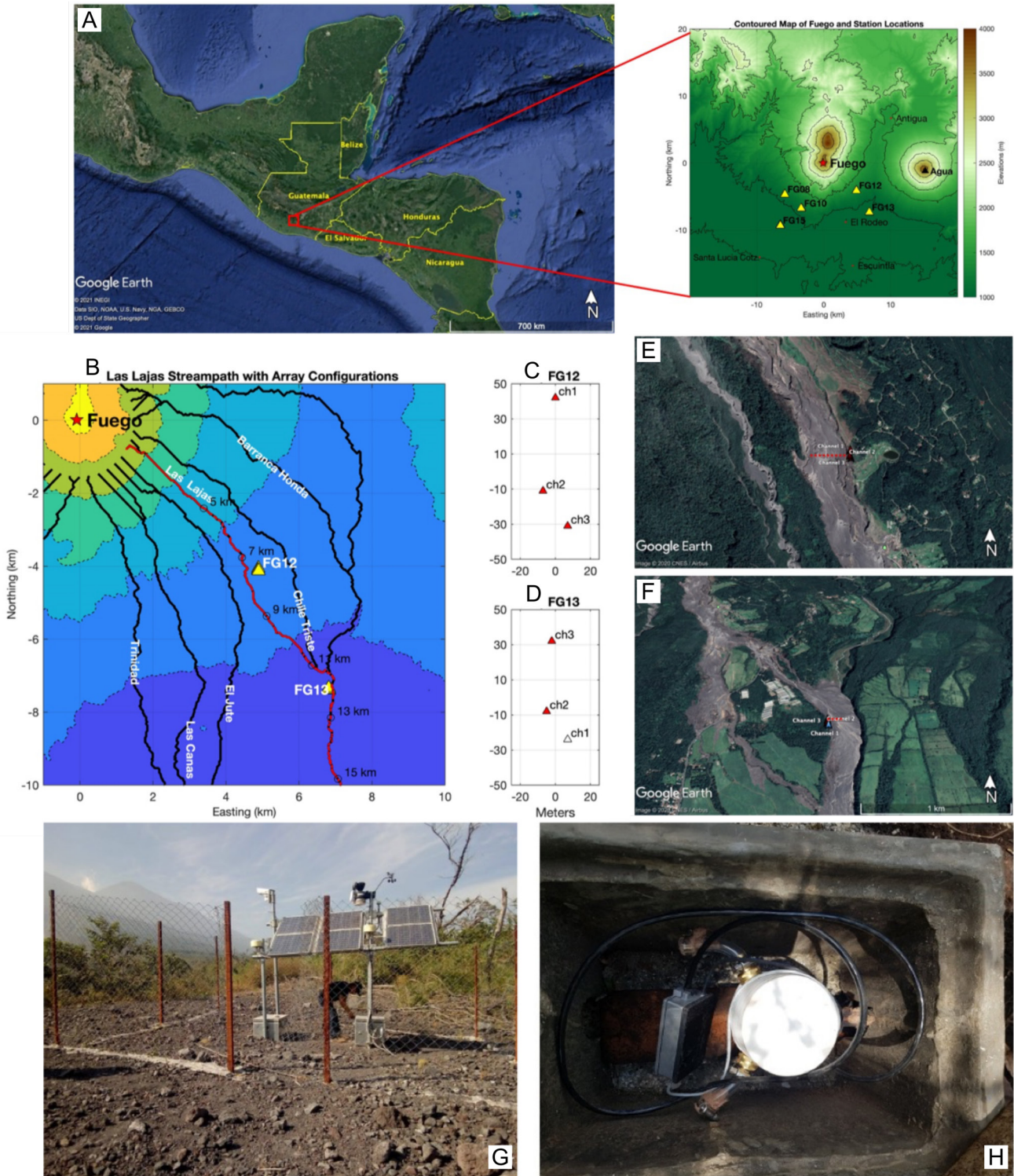
Figure 2: [A] Map of Guatemala with contoured (500m) DEM derived from SRTM showing locations of seismo-acoustic network and several population centers (inset). The Volcán de Fuego summit is indicated with a red star. [B] Drainages (thick black lines) derived from a gradient seed on a contoured SRTM DEM with the Las Lajas drainage highlighted in red. [C and D] Detailed array maps for stations FG12 and FG13, located at flow path distances of approximately 7.5 and 12 km, respectively. Channel 1 (clear triangle) at FG13 was not operational during the featured event. [E and F] Show relative distances of infrasound sensors from drainage (dashed lines represent ~200 m at FG12 (top) and ≲100 m from FG13 (bottom)) (Google Earth images from November 2018 taken by Maxar Technologies and CNES/ Airbus). [G] Infrasound station set up at FG12; [H] Infrasound sensor encased in concrete at station FG13.

event (Figure 3A–D). Various band pass ranges from as low as 0.5 Hz and above to 5 Hz and above were tested and analyzed. It was observed that our optimal cross-correlation values were achieved by filtering in the higher band (5 Hz low corner frequency). Applying a third-order median filter allows us to suppress glitches associated with lightning signals (e.g. prior to 2:30:00 UTC in Figures 3 and 4A–D), although some lightning spikes are still retained (e.g. Figure 4E–F). These are picked up by the sensor cables [e.g. Anderson et al. 2018].
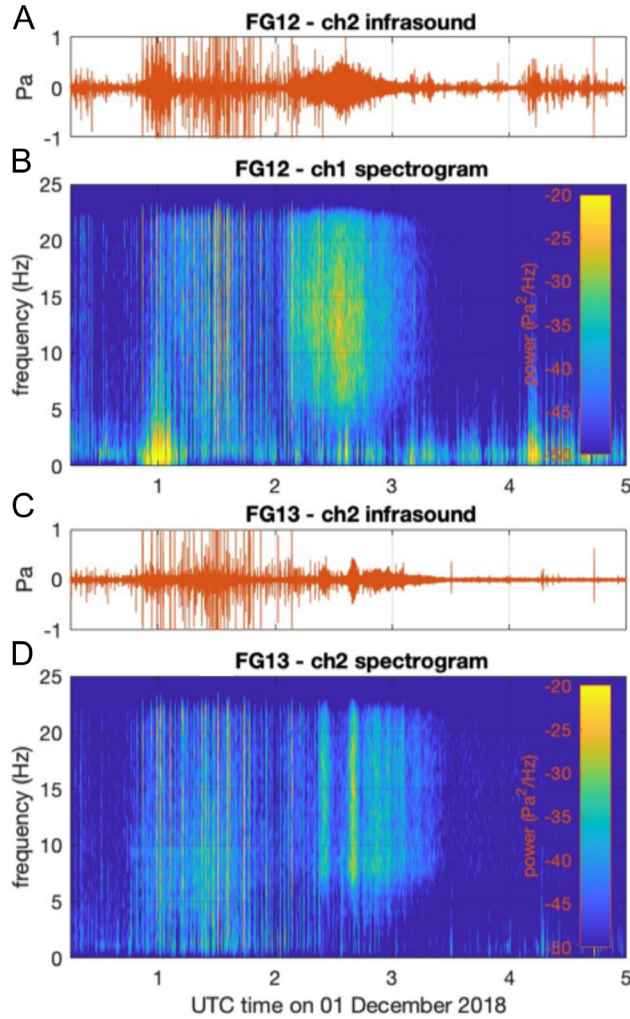
Figure 3: Spectrogram of channel 2 waveforms for both FG12 and FG13 over the entire 5-hour recorded event, including the lahar (~2:06:00 UTC to 3:05:00 UTC). The spectrogram was calculated for 10 s windows with 5 s overlaps and for infrasound data filtered above 1 Hz.

3 Methods

3.1 Lahar source tracking

We describe a method for locating lahar infrasound sources along the Las Lajas drainage. Following the methodology of Johnson and Palma [2015] we assume that candidate sources of infrasound are limited to a specific channel. Inferring that Las Lajas was the active drainage on December 01, we confine potential sources to a drainage using NASA's SRTM 30 m resolution global digital elevation model (GDEM). We identify a flow path using the DEM's steepest descent gradient starting with a source seed coordinate located 2 km ESE (120 degrees) of the summit.

We first calculate cumulative flow path distance (CFD) relative to the summit which is quantified as the integral of flow segments using Equation 1:

$$\text{CFD}(x,y,z) = \int_{2\,\text{km}}^{x,y,z} ds + 2\,\text{km} \tag{1}$$

where incremental distance elements (ds) are interpolated at 10 m spacing (Figure 2B) and calculated using Equation 2:

$$ds = \left\{ dx^2 + dy^2 + dz^2 \right\}^{1/2} \tag{2}$$

Subsequent source mapping is then measured as a function of flow distance. Although Las Lajas is the active channel for the featured lahar event in this study (based upon the prominence of recorded seismo-acoustic signals at FG12 and FG13 and absence of obvious signal at other stations), general tracking of lahars at a volcano will require consideration of other candidate drainages, each possessing its own CFD.

We next use infrasound array processing to identify which locations within Las Lajas's CFD are the most pronounced sources of infrasound. Slant distance between each possible source and all sensors in both arrays are estimated as straight-line paths. For example, the source-receiver distance from a point along the drainage to channel 1 in the FG12 array is:

$$D_{\text{FG12(1)}}(\text{CFD}) = \\ \left\{ [x - x_{\text{FG12(1)}}]^2 + \\ [y - y_{\text{FG12(1)}}]^2 + \\ [z - z_{\text{FG12(1)}}]^2 \right\}^{1/2} \tag{3}$$

where x, y, and z are the corresponding coordinates for each ds source along the Las Lajas drainage; and $x_{\text{FG12(1)}}$, $y_{\text{FG12(1)}}$, and $z_{\text{FG12(1)}}$ are the corresponding coordinates to, in this case, channel 1 at station FG12. The source-receiver wave propagation time is then calculated using a fixed sound speed:

$$t_{\text{FG12(1)}}(\text{CFD}) = \frac{D_{\text{FG12(1)}}}{c} \tag{4}$$

where the speed of sound, c, is $343\,\text{m s}^{-1}$, which corresponds to an atmosphere at ~20 °C. Propagation times are used to calculate differential travel times between
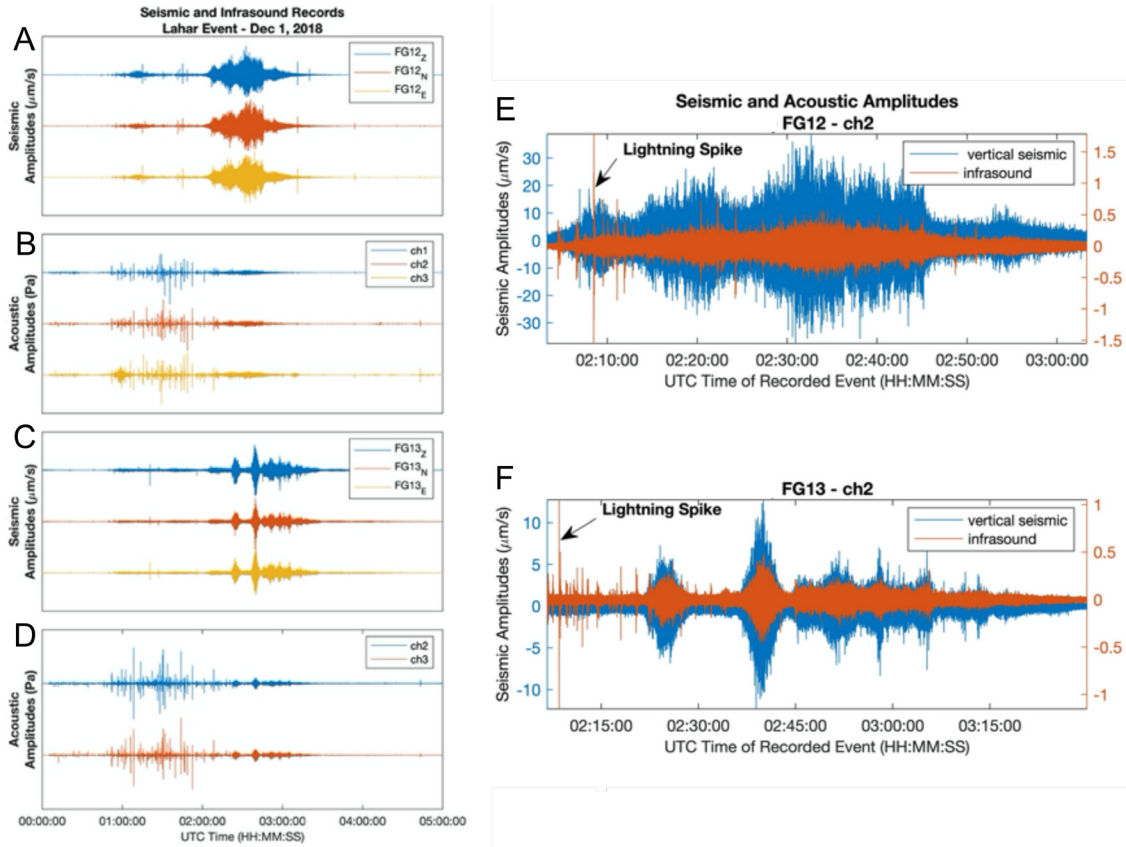
Figure 4: Seismic [A and C] and infrasound [B and D] correlated waveforms for the recorded event on 1 December 2018. Preceding the lahar event (~2:06:00−3:05:00 UTC), sensors picked up thunder and other possible storm-related noise, such as wind. [E and F] Lahar event infrasound data for channel 2 of the infrasound sensors at both stations overlain on the vertical component (z) of the seismic data. Lahar signals at both stations have a duration approximately an hour long at each station. Pulses/surges are observed in these signals and are more pronounced at FG13. Amplitudes and energy decrease for both seismic and acoustic from FG12 to FG13. Although a median filter was used to suppress noise, some lightning spikes and thunder signals were still retained.

sensor pairs within an array, for comparison to cross-correlation lag times estimated from the actual data.

As an example, the modeled differential travel time between channels 2 and 1 at FG12 is defined as

$$\delta t_{\text{FG12}(2,1)}(\text{CFD}) = t_{\text{FG12}(2)}(\text{CFD}) − t_{\text{FG12}(1)}(\text{CFD}) \quad (5)$$

where δt indicates modeled time delays. These times may then be compared to data-derived cross-correlation lag times for the same sensor pair indicated by $d\tau_{\text{FG12}(2,1)}$. Modeled differential travel times are computed for $\delta t_{\text{FG12}(2,1)}$, $\delta t_{\text{FG12}(3,2)}$, $\delta t_{\text{FG12}(1,3)}$, and $\delta t_{\text{FG13}(3,2)}$ as a function of CFD (Figure 5). Since only two infrasound sensors were functional at FG13 there is only one sensor pair of differential travel times to compute. Suboptimal detection conditions leads to potential ambiguity in source position for a two-element array but is ameliorated by the constraint that sources must be confined to the Las Lajas CFD. Note, for example in Figure 5B that a lag time of −0.1 s could locate a source at both ~11.2 and ~12.0 km CFD.

Lag times are computed from moving-window cross-correlation analysis (Figure 6A–D). In these correlograms, cross-correlation functions are plotted against time as columns with color scaled to normalized cross-correlation amplitudes. Cross-correlation analysis is performed on infrasound data after filtering between 5 and 24 Hz and applying a median filter for moving windows of length 20 s with 50 % overlap. Peak correlation values can be identified clearly despite the presence of sidelobes in the cross-correlation functions. Fit between modeled and calculated lag times are compared by computing a time residual for the three pairs in FG12, i.e.

$$\text{RMS}_{\text{FG12}}(t) =$$
$$\left\{ [\delta t_{\text{FG12}(2,1)} − \delta \tau_{\text{FG12}(2,1)}(t)]^2 + \right.$$
$$[\delta t_{\text{FG12}(3,2)} − \delta \tau_{\text{FG12}(3,2)}(t)]^2 + \quad (6)$$
$$\left. [\delta t_{\text{FG12}(1,3)} − \delta \tau_{\text{FG12}(1,3)}(t)]^2 \right\}^{1/2}.$$

For the single pair of functioning sensors in FG13, the misfit is
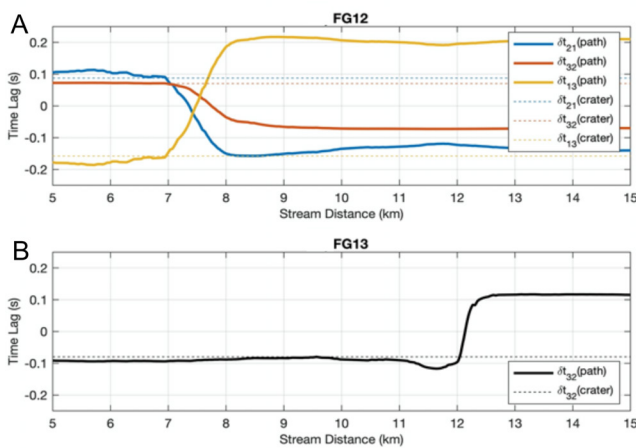
$$\text{RMS}_{\text{FG13}}(t) = \left\{ [\delta t_{\text{FG13}(3,2)} − \delta \tau_{\text{FG13}(3,2)}(t)]^2 \right\}^{1/2}. \quad (7)$$

These residuals are computed for each time step and for each candidate source location (x, y, z) within Las Lajas drainage, e.g. $x, y, z \in$ CFD. At each time step the lowest residual value is then considered the dominant source of lahar infrasound within the drainage and detected at the stations.

3.2   Lahar signal processing

Rain-triggered lahar signals, for both seismic and infrasound radiation, often have an emergent onset and spindle-shaped signal [Allstadt et al. 2018]. In the case of infrasound, we use cross-correlation of signals to identify the onset and duration of coherent lahar signals. Upsampling the correlation functions (Figure 6E–H) permits improved resolution for time lags between infrasound arriving at two sensors [Johnson and Palma 2015]. We use a factor of ten upsampling to obtain time lag variation of 2 ms derived from data with 50 Hz sample rates. The ramps evident in the five annotated pulses in Figure 6A–D each possess similar, if subtle, changes in lag times which we infer to be progression of flow pulses moving downstream adjacent to each station.

We can also use the general timing of the pulses/surges to estimate the flow speeds between the two stations. As noted by Arattano and Marchi [2008], flow fronts can be easily used to determine speed measurements between sensors or geophones at a known distance along a flow. The difference in CFD for stations FG12 and FG13 is 3.7 km (Figure 7) and we use this value coupled with pulse phase identification to calculate flow speeds for five identifiable pulse/surge

fronts within the lahar. These speeds give an overall average flow speed for the entirety of the lahar duration between the two stations.
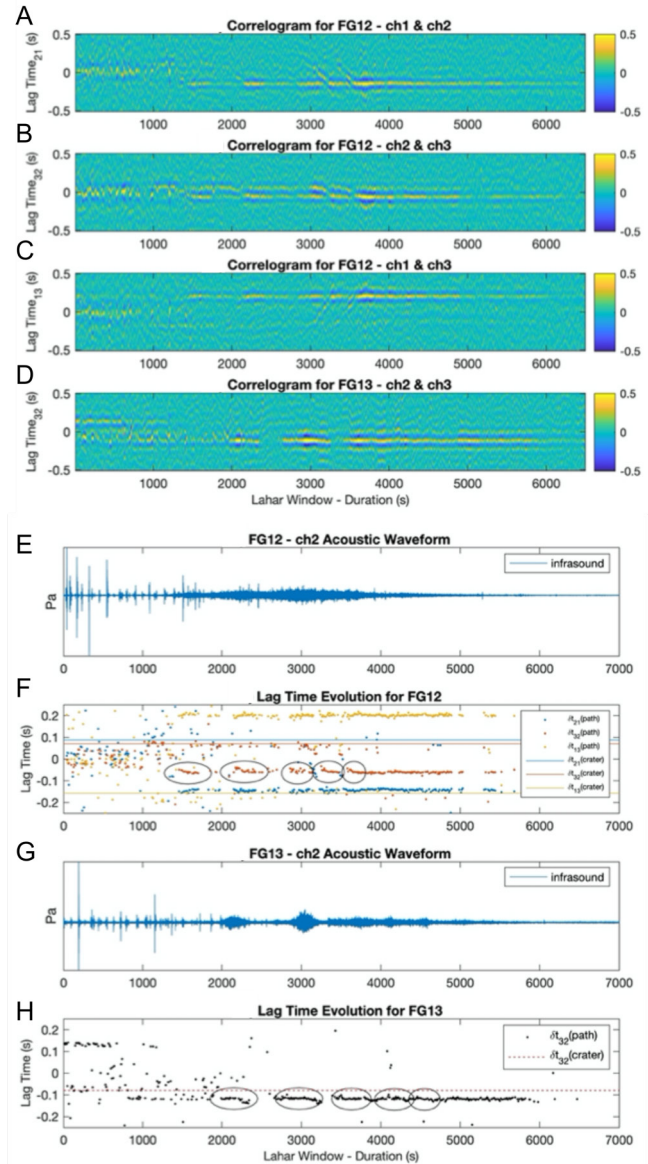
Figure 6: [A–D] Correlograms using the calculated RMS values suggest a sound source flowing from upstream to downstream. "Hotspots" (i.e. yellow) represent highly correlated signal data. [E–H] Channel 2 infrasound waveforms for both stations and cross-correlation lag time chronologies for all channel pairs within each array for the confined lahar timing window (~1420–5000 s for FG12 and ~2000–6000 s for FG13). Solid dots represent upsampled time lags from candidate sound source, compared with time lags from a point-source, such as an eruption from the summit of Volcán de Fuego (dashed lines). At least 5 pulses can be observed in both plots (circled in [F] and [H]), with the first pulse appearing approximately ~1420 s at FG12, and ~2000 s at FG13 for panels A–H.

Figure 5: Expected time delays between channels at each station from a sound source from the crater, such as an eruption (dashed lines), and a sound source from the adjacent Las Lajas drainage (solid lines). Ambiguity exists at Station FG13 at values close to -0.1 s between 11 and 11.5 km stream distance where time lag differences actually increase.

3.3 Seismic versus infrasound power

We compare the infrasound data with the co-located seismic data (Figure 4A–F) in order to better understand the relationship of infrasound to seismic power in lahars. For this comparison, we used a Seismic-Acoustic Ratio (SAR), analogous to the Volcanic Seismic-Acoustic Ratio which pertains to eruptive activity as described by Johnson and Aster [2005]. The SAR utilizes both the acoustic power (P_A) and seismic power (P_S) to characterize relative partitioning of power into the atmosphere and into the solid earth. We use the same quantification equations as in Johnson and Aster [2005] to compute signal power and then smoothed the signal power using a 2-minute window; however, to compare the evolution in seismo-acoustic power partitioning, and avoid an analysis of site response variables, we normalize the seismo-acoustic data by dividing the waveforms by a maximum value and confine the analysis to a window occurring between 2:00:00 UTC and 4:00:00 UTC. Normalizing the data scales the power levels into the same range and allows us to robustly compare variable seismic and infrasonic structures as they change over time. In order to smooth data and provide a better understanding of a broader energy relationship of the seismic and infrasound energy ratio, a relatively large median filter (120 s) was applied to the power calculations to suppress thunder signals. It should be noted that our analysis was only performed on the vertical seismic component and one channel at each station. Fluctuations in both seismo-acoustic power and SAR ratio are indicated in Figure 8A–D. For both stations, the propagation time for seismic and acoustic phases is small ($\lesssim 1$ s).

4 RESULTS

Correlated infrasound time lags correspond to source detections that map principally to positions located near the two stations FG12 and FG13 (Figure 6). This does not mean that these locations are especially intense sources of sound, but that they are preferentially detected due to proximity. In other words, due to the position of our sensors close to the lahar channel, the detected sound sources are preferentially adjacent to the stations. Notably, once the lahar has passed the stations the infrasound is not detected more than about ± 500 m CFD for FG12 and ± 200 m CFD for FG13 relative to their positions (Figures 6 and 7). This narrow range of detection argues for a more distant situation of infrasound arrays several hundred-thousands of meters away from the channel so that pulse detection corresponds to a greater sweep of CFD [e.g. Johnson and Palma 2015].

Some variation in lags (± 0.01 s) are evident for the lahar signal correlation lags and these can be attributed to detection of moving sources, which appear to move downstream. For instance, in the case of channels 3

and 2 at FG12 the lag times change at ~1420, 2180, 2880, 3250, and 3580 s (Figure 6). These lag times are converted to CFDs from 7.4 to 9 km for the first pulse and 7.6 to 9 km for subsequent pulses (Figure 7). These are interpreted as movement of transient surges, which produce higher amplitude infrasound. The slopes of the CFD time histories calculated independently for each of the three FG12 stations pairs are about $8 \, \text{m s}^{-1}$, which can be interpreted as the speed of the surges at that station.

FG13 lag time evolution for channels 2 and 3 also hints at movement of a pulse from upstream to downstream (Figure 6). The interpreted locations change from about 11.2 to 11.5 km CFD for each of the pulses (Figure 6). This variation in location is less than that of FG12 possibly because those sensors are located closer to the location of the active flow path and are most sensitive to nearby sound sources. Also, because FG13 is a two-element array the conversion between lag time and CFD position is ambiguous between about 11 and 12 km: the same lag time could correspond to two positions on the CFD. This ambiguity argues for the importance of using three or more elements in tracking sources using infrasound.

We compare cross-correlated signals and pulse timing at FG12 and FG13 to estimate the duration and speed of flow during the 1 December 2018 lahar event for the transect between FG12 and FG13 (from ~7.4 to ~11.5 km). We use highly correlated signals ("hotspots") in Figure 6A–D to identify the start and end of the lahar, calculating a little over an hour duration at each station. The five pulses in Figure 7 are identifiable and can be visually correlated to understand the movement of the pulses between the two stations. These pulse speeds appear to decrease over time: from 8.3 to 7.0, 6.6, 6.5, and then $6.3 \, \text{m s}^{-1}$. The average overall speed over the duration of the lahar was approximately $6.9 \, \text{m s}^{-1}$. These flow speeds are in agreement with previously reported values [Pierson 1985; Johnson and Palma 2015; Allstadt et al. 2018], and also reasonable for secondary discrete pulses, which commonly travel slower than the front of the lahar [Doyle et al. 2011].

The energetics of the seismic and infrasonic records indicate clear pulses in source intensity that correlate with the pulses passing adjacent to each station (Figure 8A and 8C). These pulses appear more distinct at FG13 than at FG12. At both stations, the seismic energy peak precedes the peak in infrasonic energy by 90 s. The ratios (as shown in Figure 8B and 8D) were close to 1, indicating little variability in the normalized SAR at both stations. It is notable that the seismic and infrasonic energy time series are highly correlated (Figure 8A and 8C).
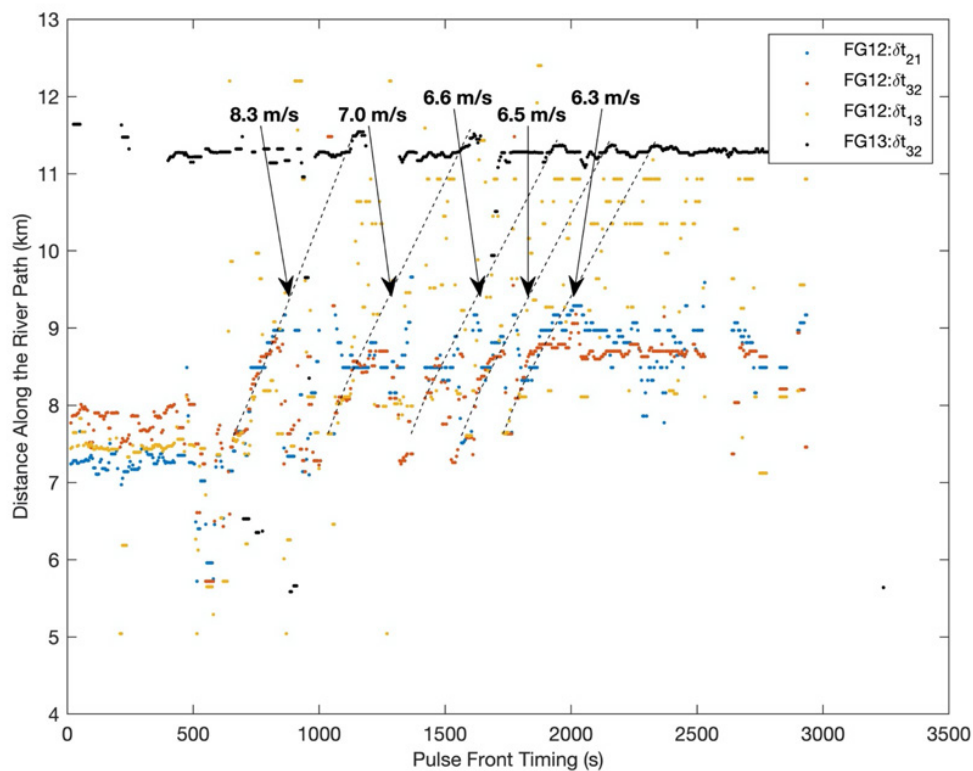
Figure 7: Flow pulse identification at FG12 and FG13. Dashed lines designate the beginning of pulses/surges at both stations as they travel downstream. Calculated flow speeds between FG12 and FG13 show a decrease from 8.3 to 6.3 m^{-1} over the course of these surges. Refer to Figure 3 for differences in starting times between FG12 and FG13. The y-axis is converted to CFD for each station. The timeline in this figure has been truncated along the x-axis and only high-quality correlations between the data have been plotted for better visualization of the pulses within the lahar. The detectability window of these pulses at both stations is 7.4–9 km at FG12, and 11.2–11.5 km at FG13.

5 Discussion

The initial results from this study demonstrate the chronology of a single multi-pulsed lahar event at Volcán de Fuego using both infrasound and seismic signals. We interpret these signals as a flow that moves at an average speed of about 6.9 ± 1 m s^{-1} and as a series of pulses between stations FG12 and FG13. We suggest that pulses may arise from flow transitions between debris flows and more dilute, hyperconcentrated flows as it travels downstream. Progression and transition of debris flows to hyperconcentrated flows has been observed in other rain-triggered lahars [Pierson 1985; Lavigne and Suwa 2004]. The liquid-solid interaction within lahars is complex and can be highly variable due to bulking, debulking, dilution and infiltration [Fagents and Baloga 2006; Jones et al. 2015; Walsh et al. 2020]. Flow behavior of lahars depends on the amount, type and size distribution of the entrained sediment [Fagents and Baloga 2006], with hyperconcentrated flows producing more turbulent transport, and small yield strength [Pierson and Costa 1987; Walsh et al. 2020], while debris flows behave as a coherent, plas-

tic mass, with turbulence dampened [Pierson and Costa 1987] and high yield strength.

5.1 Controls on pulses

Recorded signals exhibit multiple pulses reflected in the increasing and decreasing seismic and acoustic amplitudes over time scales of the order of ten minutes. These are evident in both FG12 and FG13 signals, however, their nature is different between the stations, with more defined and pronounced fluctuations in the waveforms occurring at FG13 (Figure 4E–F). It is common for lahars to develop pulses as the flow progresses downstream due to bulking/debulking processes and fluctuations of erosion and aggradation through space and time [Zanuttigh and Lamberti 2007; Doyle et al. 2010]. The fluctuations in flow dynamics are consistent with transitional phases between a concentrated debris flow head, followed by a hyperconcentrated flow tail (Figure 1). The fact that both seismic and infrasonic energy fluctuate with each pulse suggests either oscillations in material flux, flow speed, and/or flow concentration. Channel bed composition and channel ge-
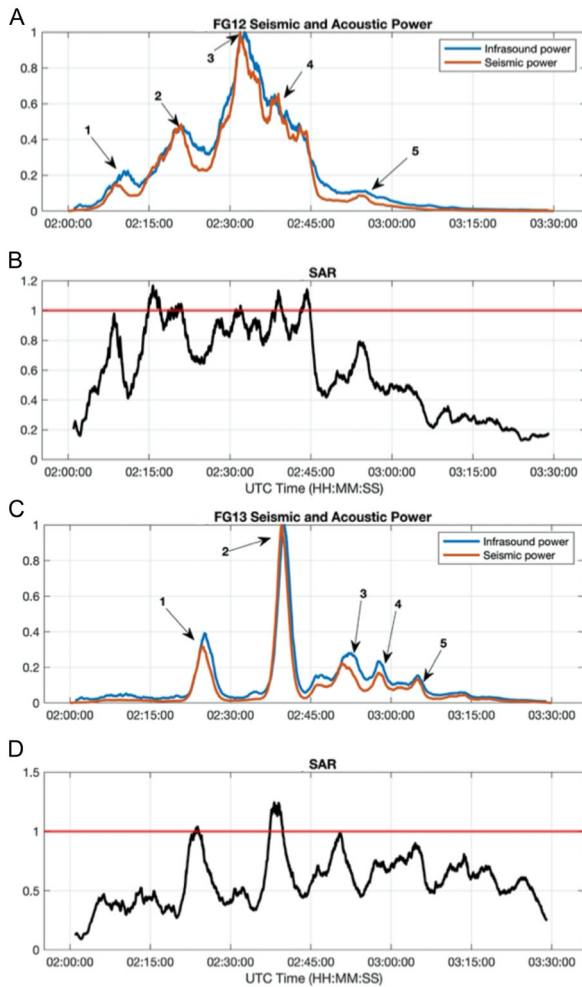
Figure 8: [A–D] Power differences ([A] and [C]) and Seismic-Acoustic Ratio, SAR ([B] and [D]) for their respective stations in relation to the energetics of the lahar event. The red line in B and D indicates a ratio equal to 1. The five identified pulses from Figure 5E−F have been numbered here for each station ([A] and [C]). Note the similarity between the seismic and infrasound, and the pronounced energy for both seismic and infrasound at FG13 ([C] and [D]). In order to smooth data and provide a better understanding of a broader energy relationship of the seismic and infrasound energy ratio, a relatively large median filter (120 s) was applied to the power calculations to suppress thunder signals.

ometry may also impact energy fluctuations observed in the pulses [Huang et al. 2004; Walsh et al. 2020]. We also investigate the energy relationships of seismic and infrasonic signals for each pulse (Figure 8A and 8C). Our hypothesis is that sediment load may play a role in differences between seismic energy and infrasonic radiation. In this case, the debris-laden lahars might produce more seismic energy, where the bulk of the sediment load and boulders is concentrated at the steep, lobate snout of the flow [Doyle et al. 2011; Gimbert et al. 2014; Vallance and Iverson 2015], and imparts pref-

erentially more energy to the solid earth (i.e. ground vibrations). Conversely, a more dilute, hyperconcentrated flow, with lower gross density, may impart less stresses to the ground. We assume infrasound is produced by lahar-air interactions of breaking waves as a result of interactions between clasts within the flow [Schmandt et al. 2013] or the composition of the channel bed [Huang et al. 2004; Walsh et al. 2020] and these probably increase with flow speed and variations with material flux.

5.2 Flow evolution from FG12 to FG13

Pronounced differences in seismo-acoustic signals between FG12 and FG13 could be due to variations in flow speed and sediment load as the lahar travels downstream. By 'pronounced,' we mean to say the pulses are relatively diffused at FG12 compared to FG13. Related to this, mean absolute amplitude of seismic speed and infrasound pressure records decrease from station FG12 to FG13 (Figure 4E–F), e.g. $3.87\,\mu m\,s^{-1}$ and $0.051\,Pa$ at FG12 and $0.62\,\mu m\,s^{-1}$ and $0.030\,Pa$ at FG13. Notwithstanding potential differences due to source-receiver distances at FG12 and FG13 between flow path and station, these systematic decreases argue for diminished flow energetics.

These amplitude and energy decreases are reasonable considering the change in slope steepness between the two stations (Figure 9). The average slope in the vicinity of FG12 and FG13 are about 5 degrees and 3 degrees respectively and may contribute to a diminished flow speed at FG13. Furthermore, the channel widens considerably just north of FG13, and a change in channel geometry may account for differences in the flow energetics between the two stations [e.g. Coviello et al. 2019; Marchetti et al. 2019]. Doyle et al. [2010] notes that, in general, increased seismic amplitude and energies correlates to volume concentration increases. Therefore, we infer that a higher seismic amplitudes and energies seen at station FG12 could also indicate a larger sediment load than near FG13.

There are several factors which may account for a flow regime transition along the Las Lajas drainage just north of station FG13. The first may be a confluence with the Chile Triste and Barranca Honda (barranca is the Spanish term for a deep gully or arroyo, akin to a drainage) tributaries into the main channel of the Las Lajas (Figure 2B). Addition of water from sources such as these can decrease the carrying capacity of the flow, which dilutes the system, leading to greater debulking of particles out of the system [Fagents and Baloga 2006]. The second explanation for a transition in flow may be the sudden widening of the river channel, which could control flow speed and cross-sectional flow profile (e.g. flow depth) [Figure 9; Pierson 1985; Fagents and Baloga 2006]. The stream path near FG12 is more confined and travels through shallow canyons, until it is just upstream from FG13 (Figure 9). At this

point, Las Lajas merges with Barranca Honda and the river channel widens considerably, and also decreases in slope by 1–2°. Widening of the channel with simultaneous stream slope decrease creates a drop in flow energy and grain settlement will increase. High sediment load and deposition is evident in the appearance of braided streams adjacent to and downstream from FG13 (Figure 9E). As a consequence of this de-bulking process, it is common to observe non-cohesive debris flows transitioning to hyperconcentrated flows as the system energy abates due to decreases in slope steepness [Figure 9; Pierson 1985; Lavigne and Suwa 2004; Capra et al. 2010; Doyle et al. 2011; Capra et al. 2018], resulting in progressive settling out of particles from the flow. A combination of some or all of these processes may be taking place as the lahar approaches FG13, resulting in the variations in signals observed in our data.

Previous research on other types of gravity-driven mass-wasting events has been capable of extracting aspects of flow dynamics utilizing seismic data [e.g. Huang et al. 2007; Moretti et al. 2012; Allstadt 2013; Lai et al. 2018], and research on fluvial seismology has delineated flow characteristics in ground vibrations [e.g. Rickenmann et al. 2012; Schmandt et al. 2013; Gimbert et al. 2014; Burtin et al. 2016]. We use these studies as a basis for interpretation in our own data. The overall similarity in seismo-acoustic energy envelopes suggest that processes associated with variable flow energetics are radiated both seismically and infrasonically. In controlled fluvial experiments, Schmandt et al. noted seismo-acoustic power increases that aligned specifically in the band around 6.25 Hz and inferred water-air interactions were correlated with bed-load movement during peak discharges. In another study by Huang et al. [2007], certain frequencies of ground vibrations in seismic data correlated to interaction of entrained rocks or boulders with the channel bed at the front of debris flows. It has also been observed that the nature and geometry of the channel also plays a role in the amplitudes and frequencies produced by debris flows with a similar effect on lahar seismic signals [e.g. Huang et al. 2004; Lai et al. 2018; Thouret et al. 2020], although these parameters were unavailable to us during this featured study. Other seismic and infrasound studies have noted that larger clasts [Chou et al. 2007] and a boulder-rich surge front [Zanuttigh and Lamberti 2007; Doyle et al. 2010; Kean et al. 2015] are responsible for higher frequency seismo-acoustic energy and higher amplitude signals than the intersurge flow, respectively (Figure 1). Other studies have also inferred variable frequency responses relate to differences in flow concentrations and changes in channel geometry which influence characteristics seen in seismic flow signals [e.g. Marcial et al. 1996; Cole et al. 2009; Marchetti et al. 2019; Walsh et al. 2020], although correlations between sediment transport and acoustic signals remain poorly

understood. Moving forward, field correlation between macroscopic flow observables and seismo-acoustic energetics is needed to ascertain the connection between energy and sediment characteristics and concentrations within lahars. Therefore, spectral analysis will be considered in future lahar studies at Volcán de Fuego as a means of describing these types of energy relationships.

Notably, the FG13 array primarily detects signals upstream, whereas FG12 detects lahar signals both upstream and downstream. We highlight that station FG13 observed no signals downstream of the 11.5 km CFD after each pulse (Figure 6B), indicating that the sound source could not be detected downstream from this station. Lack of downstream detection at this station suggests that sound sources are preferentially detected upstream and to the north of FG13, and reflects detections which are most energetic and/or closest [Kudo 1993; Marchetti et al. 2019]. Previous work has proposed that infrasound sources may be fixed at locations such as waterfalls and rapids or at least in areas of greatest flow energetics [Kudo 1993; Marchetti et al. 2019]. This was supported by Johnson and Palma [2015] who located lahar sound sources that were stationary after an initial period when the lahar advanced. The topography of the Las Lajas drainage just north of the FG13 array, before the channel widens, is hilly and complex (Figure 9), with moderate slope, possible rapids and fast-moving flow. It is also prudent to note that just north of FG13, where most of the array's coherent infrasound originates, sudden widening of the river channel and probable hydraulic jump could account for a disproportionate share of both seismic and acoustic power at station FG13 [Figure 9B–E Ronan et al. 2017; Marchetti et al. 2019]. Without visual ground truth, however, it is hard to say whether these flow behaviors occurred during this lahar event.

Lack of resolution in detecting advancing flow pulses using infrasound is due in part to the location of the arrays very close to the edge of the lahar paths. Because the arrays are so close to the infrasound source the signals preferentially record adjacent hydraulic activity. We suggest that the location of infrasound sensors farther away from the channel (several hundreds of meters to kilometers [e.g. Johnson and Palma 2015] would probably provide better resolving capability for tracking advancing pulses.

5.3   Future directions

While this study shows promise in using infrasound in lahar detection and tracking, describing flow characteristics would be complemented by use of visual resources (e.g. time-lapse cameras). For instance, time-lapse imagery at Volcán de Fuego for a different lahar and drainage (Figure 10) shows dynamic flow behavior where multiple pulses are observed as rising and falling flow stages over time scales of 10–15 minutes. We propose that these fluctuations may be similar to the pulses
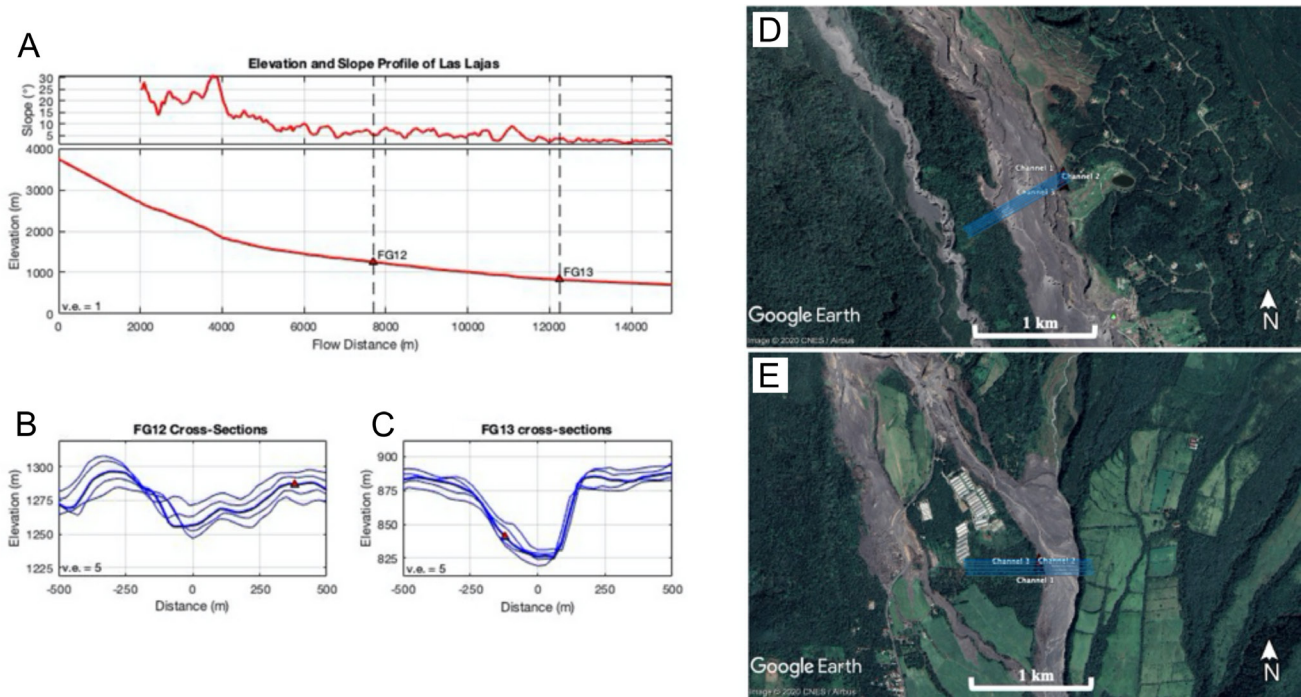
Figure 9: [A] Slope profile along Las Lajas drainage shows a slight change in slope angle from 5–8°at FG12 to approximately 2–4°at FG13. [B] and [C] Cross-sectional profiles with station locations (red triangles) correspond to NE-W and E-W slope profiles (blue lines) on Google Earth images ([D] and [E]). [D] and [E] Google Earth images from November 2018 taken by Maxar Technologies and CNES/ Airbus.

analyzed in the featured event from Las Lajas and described in Section 5.2. Visual images not only aid us in observing changing flow behaviors (Figure 10) but can also be used for calculations of surface speed and stage measurements [Lavigne and Thouret 2003; Doyle et al. 2010], which can augment flow mass and volume flux estimates. Observed infrasound characteristics can also be correlated to visual data, enhancing our understanding about how flow behaviors in lahars influence infrasound wave generation. Further calculations of the SAR may serve to highlight preferential wave propagation within the lahar based on the evolution of flow type regime and/or sediment load if a definitive dynamic change exists. Elastic energies may also provide an observation for quantifying lahar parameters and intensity, in the broader context, and comparison for a suite of lahar events. These parameters may then be utilized in early warning systems as a way to characterize the types and intensities of flows that may inundate lower-lying areas. Additionally, complementary instrumentation such as rain gauges could be integrated into future work to help calibrate and fine-tune monitoring systems and delineate impacts of rainfall on triggering mechanisms and/or pulse formation. Given the large geographic extent of Volcán de Fuego, rainfall variations across even the same drainage must be taken into account when assessing differences in flow behaviors occurring both proximally and distally to the volcano. We also argue that moving the location of the sensors farther from the drainage can give a bet-

ter range of back azimuths. This is not only true for the detection and tracking of lahars but has the potential for also tracking PDCs as they travel through the drainages during larger eruptions. Continuous examinations and monitoring of these rain-triggered lahars at Volcán de Fuego will help quantify and characterize further flow behaviors through a comprehensive ensemble dataset. We believe geophysical monitoring using combined seismo-infrasonic observations is fundamental in understanding lahar hazards, risk, and impacts on human populations.

CONCUSIONS

Seismic and acoustic analysis of a lahar in the Las Lajas drainage on Volcan de Fuego, Guatemala, reveals variability in flow characteristics over the hour-long event. We identify five pulses and argue that varying sediment load is reflected by clear fluctuations in infrasound and seismic power recorded at one of the stations. Infrasound can be utilized, much like seismic data, to calculate flow parameters such as the timing of the flow, the duration of the lahar, and the flow speeds of each pulse. We have shown that single arrays can be used to calculate velocities of pulses as lahars move downstream, adjacent to, and downstream of each station; however, multiple arrays should be used to translate the speed of the entire flow between stations. We have also demonstrated that although a sensor was dam-
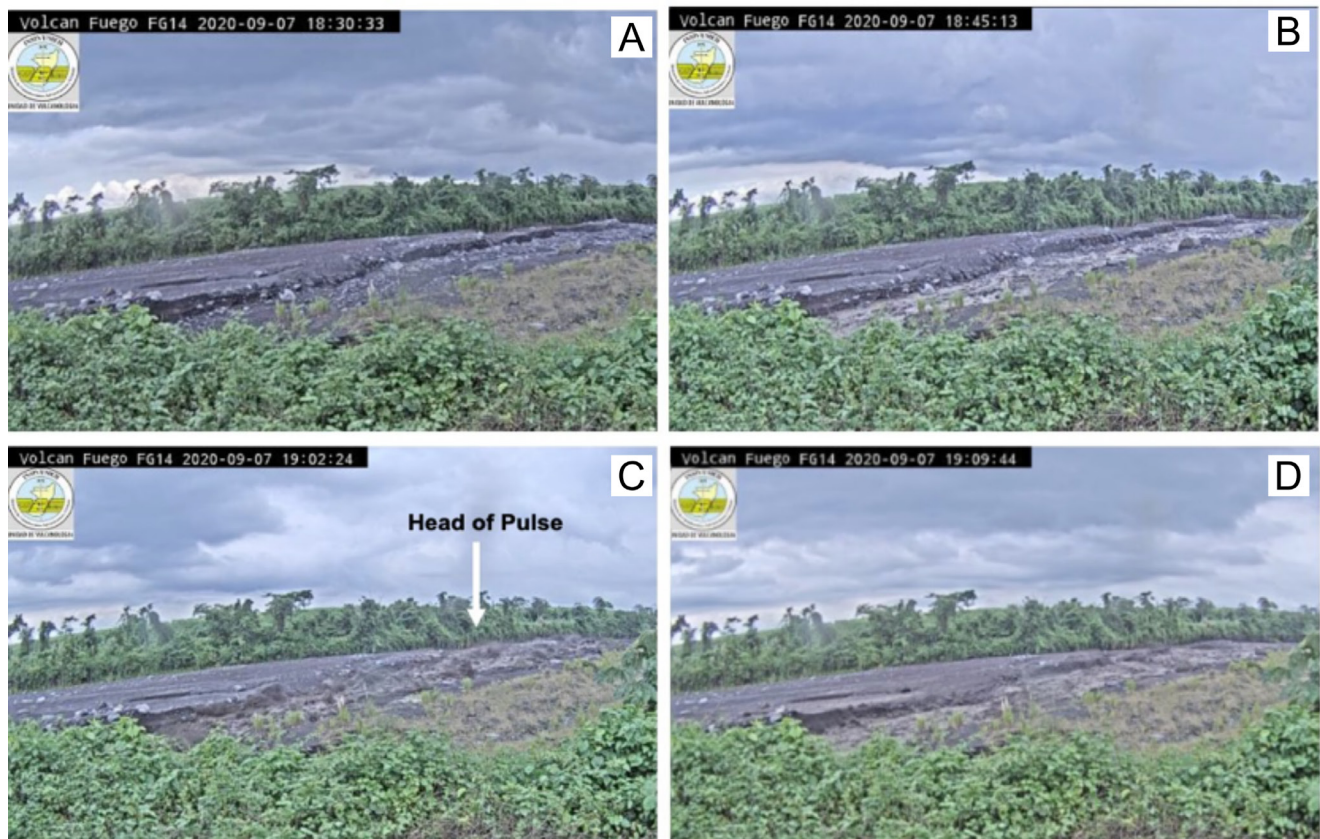
Figure 10: An example of INSIVUMEH time lapse footage of a lahar with pulses in the Ceniza drainage on 7 September 2020. [A] 18:30:33 local time: normal streamflow within the river channel. [B] 18:45:13: first pulse as a lahar coming down the channel increases streamflow height. [C] 19:02:24: a larger, second pulse starts to inundate the area and overbanks the confined river channel as it flows past the camera. [D] 17:09:44: water recedes as the tail of the second pulse passes; however, turbulence can still be seen with surface waves. A third pulse was also observed at 19:11:44 (not shown), before the water receded back to normal streamflow.

aged at the FG13 array and non-operational during this event, the method for detecting and tracking lahars can still be used even under suboptimal conditions, as we were able to calculate time lag differences between two of the sensors and identify pulses within the flow. When compared with the seismic records, infrasound signal analysis reinforces the importance and utility of this technology to detect and track rain-triggered lahars, as well as to quantify the hydrological and geomorphic parameters that characterize these types of flows. Although the energy relationships between seismic and infrasound did not vary significantly within this lahar, this comparison method can be used as a tool to quantify energy relationships across a much larger dataset.

Author contributions

Ashley Bosa wrote the manuscript and conceptualized and analyzed the seismo-acoustic data with assistance from Jeffrey Johnson, who also provided conceptualization and funding acquisition. Silvio De Angelis and John Lyons provided seismo-acoustic data and metadata with instructions on acquisition parameters, as well as reviewing and editing. Our colleague at IN-

SIVUMEH, Amilcar Roca, provided invaluable information about local topography and sensor set-up, photos of sensors and stations and time-lapse videos from other lahar events, as well as reviewing and editing. Jacob Anderson presented insight on hydraulic jumps and infrasound signal characteristics, as well as reviewing and editing. Armando Pineda provided invaluable information about local topography, accessibility for future deployments, and discussions about impacted communities, and reviewing the manuscript.

DATA AVAILABILITY

The seismo-acoustic waveforms analyzed here are available for public download from a Boise State University ScholarWorks archive focused on infrasound datasets https://scholarworks.boisestate.edu/infrasound_data/; https://doi.org/10.18122/infrasound_data/6/boisestate. Digital elevation models were obtained from NASA Shuttle Radar Topography Mission (SRTM) Version 3.0 Global 1 arc-second resource.

COPYRIGHT NOTICE

REFERENCES

Allstadt, K. E. (2013). "Extracting source characteristics and dynamics of the August 2010 Mount Meager landslide from broadband seismograms". *Journal of Geophysical Research: Earth Surface* 118.3, pp. 1472–1490. DOI: 10.1002/jgrf.20110.

Allstadt, K. E., M. Farin, A. B. Lockhart, S. K. McBride, J. W. Kean, R. M. Iverson, M. Logan, J. B. Smith, V. C. Tsai, and D. George (2019). "Overcoming barriers to progress in seismic monitoring and characterization of debris flows and lahars". *Debris-Flow Hazards Mitigation: Mechanics, Monitoring, Modeling, and Assessment*. Ed. by J. W. Kean, J. A. Coe, P. M. Santi, and B. K. Guillen. Mountain Scholar. DOI: 10.25676/11124/173234.

Allstadt, K. E., R. S. Matoza, A. B. Lockhart, S. C. Moran, J. Caplan-Auerbach, M. M. Haney, W. A. Thelen, and S. D. Malone (2018). "Seismic and acoustic signatures of surficial mass movements at volcanoes". *Journal of Volcanology and Geothermal Research* 364, pp. 76–106. DOI: 10.1016/j.jvolgeores.2018.09.007.

Anderson, J. F., J. B. Johnson, A. L. Steele, M. C. Ruiz, and B. D. Brand (2018). "Diverse Eruptive Activity Revealed by Acoustic and Electromagnetic Observations of the 14 July 2013 Intense Vulcanian Eruption of Tungurahua Volcano, Ecuador". *Geophysical Research Letters* 45.7, pp. 2976–2985. DOI: 10.1002/2017gl076419.

Arattano, M. and L. Marchi (2008). "Systems and Sensors for Debris-flow Monitoring and Warning". *Sensors* 8.4, pp. 2436–2452. DOI: 10.3390/s8042436.

Beverage, J. P. and J. K. Culbertson (1964). "Hyperconcentrations of Suspended Sediment". *Journal of the Hydraulics Division* 90.6, pp. 117–128. DOI: 10.1061/jyceaj.0001128.

Burtin, A., N. Hovius, and J. M. Turowski (2016). "Seismic monitoring of torrential and fluvial processes". *Earth Surface Dynamics* 4.2, pp. 285–307. DOI: 10.5194/esurf-4-285-2016.

Cando-Jácome, M. and A. Martínez-Graña (2019). "Determination of Primary and Secondary Lahar Flow Paths of the Fuego Volcano (Guatemala) Using Morphometric Parameters". *Remote Sensing* 11.6, p. 727. DOI: 10.3390/rs11060727.

Capra, L., L. Borselli, N. Varley, J. Gavilanes-Ruiz, G. Norini, D. Sarocchi, L. Caballero, and A. Cortes (2010). "Rainfall-triggered lahars at Volcán de Colima, Mexico: Surface hydro-repellency as initiation process". *Journal of Volcanology and Geothermal Research* 189.1-2, pp. 105–117. DOI: 10.1016/j.jvolgeores.2009.10.014.

Capra, L., V. Coviello, L. Borselli, V.-H. Márquez-Ramírez, and R. Arámbula-Mendoza (2018). "Hydrological control of large hurricane-induced lahars: evidence from rainfall-runoff modeling, seismic and video monitoring". *Natural Hazards and Earth System Sciences* 18.3, pp. 781–794. DOI: 10.5194/nhess-18-781-2018.

Chou, H. T., Y. L. Cheung, and S. C. Zhang (2007). "Calibration of infrasound monitoring system and acoustic characteristics of debris-flow movement by field studies". *Debris-flow hazards mitigation: mechanics, prediction, and assessment*. Ed. by C. L. Chen and J. J. Major. Rotterdam: Millpress Science Publishers, pp. 571–580. ISBN: 978-90-5966-059-5.

Cole, S. E., S. J. Cronin, S. Sherburn, and V. Manville (2009). "Seismic signals of snow-slurry lahars in motion: 25 September 2007, Mt Ruapehu, New Zealand". *Geophysical Research Letters* 36.9. DOI: 10.1029/2009gl038030.

Coviello, V., M. Arattano, F. Comiti, P. Macconi, and L. Marchi (2019). "Seismic Characterization of Debris Flows: Insights into Energy Radiation and Implications for Warning". *Journal of Geophysical Research: Earth Surface* 124.6, pp. 1440–1463. DOI: 10.1029/2018jf004683.

Coviello, V., L. Capra, R. Vázquez, and V. H. Márquez-Ramírez (2018). "Seismic characterization of hyperconcentrated flows in a volcanic environment". *Earth*

Surface Processes and Landforms 43.10, pp. 2219–2231. DOI: 10.1002/esp.4387.

De Angelis, S., A. Diaz-Moreno, and L. Zuccarello (2019). "Recent Developments and Applications of Acoustic Infrasound to Monitor Volcanic Emissions". *Remote Sensing* 11.11, p. 1302. DOI: 10.3390/rs11111302.

Diaz-Moreno, A., A. Roca, A. Lamur, B. H. Munkli, T. Ilanko, T. D. Pering, A. Pineda, and S. De Angelis (2020). "Characterization of Acoustic Infrasound Signals at Volcán de Fuego, Guatemala: A Baseline for Volcano Monitoring". *Frontiers in Earth Science* 8. DOI: 10.3389/feart.2020.549774.

Doyle, E. E., S. J. Cronin, S. E. Cole, and J.-C. Thouret (2010). "The coalescence and organization of lahars at Semeru volcano, Indonesia". *Bulletin of Volcanology* 72.8, pp. 961–970. DOI: 10.1007/s00445-010-0381-8.

Doyle, E. E., S. J. Cronin, and J.-. C. Thouret (2011). "Defining conditions for bulking and debulking in lahars". *Geological Society of America Bulletin* 123.7-8, pp. 1234–1246. DOI: 10.1130/b30227.1.

Dumaisnil, C., J.-C. Thouret, G. Chambon, E. E. Doyle, S. J. Cronin, and Surono (2010). "Hydraulic, physical and rheological characteristics of rain-triggered lahars at Semeru volcano, Indonesia". *Earth Surface Processes and Landforms* 35.13, pp. 1573–1590. DOI: 10.1002/esp.2003.

Fagents, S. A. and S. M. Baloga (2006). "Toward a model for the bulking and debulking of lahars". *Journal of Geophysical Research* 111.B10. DOI: 10.1029/2005jb003986.

Fee, D. and R. S. Matoza (2013). "An overview of volcano infrasound: From hawaiian to plinian, local to global". *Journal of Volcanology and Geothermal Research* 249, pp. 123–139. DOI: 10.1016/j.jvolgeores.2012.09.002.

Flynn, I. T. W. and M. S. Ramsey (2020). "Pyroclastic Density Current Hazard Assessment and Modeling Uncertainties for Fuego Volcano, Guatemala". *Remote Sensing* 12.17, p. 2790. DOI: 10.3390/rs12172790.

Gimbert, F., V. C. Tsai, and M. P. Lamb (2014). "A physical model for seismic noise generation by turbulent flow in rivers". *Journal of Geophysical Research: Earth Surface* 119.10, pp. 2209–2238. DOI: 10.1002/2014jf003201.

Global Volcanism Program (2013). "Volcanoes of the World, v. 4.3.4". Ed. by E. Venzke. DOI: 10.5479/si.gvp.votw4-2013.

– (2018). "Report on Fuego (Guatemala)". *Bulletin of the Global Volcanism Network* 43.8. Ed. by E. Venzke. DOI: 10.5479/si.gvp.bgvn201808-342090.

– (2019). "Report on Fuego (Guatemala)". *Bulletin of the Global Volcanism Network* 44.10. Ed. by A. E. Crafford and E. Venzke. DOI: 10.5479/si.gvp.bgvn201910-342090.

Hadley, K. C. and R. G. LaHusen (1995). *Technical manual for the experimental acoustic flow monitor*. Tech. rep. Open-File Report 95-114.

Huang, C.-J., C.-L. Shieh, and H.-Y. Yin (2004). "Laboratory study of the underground sound generated by debris flows". *Journal of Geophysical Research: Earth Surface* 109.F1. DOI: 10.1029/2003jf000048.

Huang, C.-J., H.-Y. Yin, C.-Y. Chen, C.-H. Yeh, and C.-L. Wang (2007). "Ground vibrations produced by rock motions and debris flows". *Journal of Geophysical Research* 112.F2. DOI: 10.1029/2005jf000437.

Iverson, R. M., M. Logan, R. G. LaHusen, and M. Berti (2010). "The perfect debris flow? Aggregated results from 28 large-scale experiments". *Journal of Geophysical Research* 115.F3. DOI: 10.1029/2009jf001514.

Janda, R. J., A. S. Daag, P. Delos Reyes, C. G. Newhall, T. C. Pierson, R. S. Punongbayan, K. S. Rodolfo, R. U. Solidum, and J. V. Umbal (1996). "Assessment and response to lahar hazard around Mount Pinatubo, 1991 to 1993". *Fire and mud: Eruptions and lahars of Mount Pinatubo, Philippines*. Ed. by C. G. Newhall and R. Punongbayan. Philippine Institute of Volcanology, Seismology, and Seattle University, pp. 107–140.

Johnson, J. B. and R. C. Aster (2005). "Relative partitioning of acoustic and seismic energy during Strombolian eruptions". *Journal of Volcanology and Geothermal Research* 148.3-4, pp. 334–354. DOI: 10.1016/j.jvolgeores.2005.05.002.

Johnson, J. B. and J. L. Palma (2015). "Lahar infrasound associated with Volcán Villarrica's 3 March 2015 eruption". *Geophysical Research Letters* 42.15, pp. 6324–6331. DOI: 10.1002/2015gl065024.

Johnson, J. B., L. M. Watson, J. L. Palma, E. M. Dunham, and J. F. Anderson (2018). "Forecasting the Eruption of an Open-Vent Volcano Using Resonant Infrasound Tones". *Geophysical Research Letters* 45.5, pp. 2213–2220. DOI: 10.1002/2017gl076506.

Jones, R., V. Manville, and D. Andrade (2015). "Probabilistic analysis of rain-triggered lahar initiation at Tungurahua volcano". *Bulletin of Volcanology* 77.8. DOI: 10.1007/s00445-015-0946-7.

Jones, R., R. E. Thomas, J. Peakall, and V. Manville (2017). "Rainfall-runoff properties of tephra: Simulated effects of grain-size and antecedent rainfall". *Geomorphology* 282, pp. 39–51. DOI: 10.1016/j.geomorph.2016.12.023.

Kataoka, K. S., T. Matsumoto, T. Saito, K. Kawashima, Y. Nagahashi, T. Iyobe, A. Sasaki, and K. Suzuki (2018). "Lahar characteristics as a function of triggering mechanism at a seasonally snow-clad volcano: contrasting lahars following the 2014 phreatic eruption of Ontake Volcano, Japan". *Earth, Planets and Space* 70.1. DOI: 10.1186/s40623-018-0873-x.

Kean, J. W., J. A. Coe, V. Coviello, J. B. Smith, S. W. McCoy, and M. Arattano (2015). "Estimating rates of debris flow entrainment from ground vibrations". *Geo-*

physical Research Letters 42.15, pp. 6365–6372. DOI: 10.1002/2015gl064811.

Kudo, N. (1993). "Control of Infrasonic Noise from a Waterfall". *Journal of Low Frequency Noise, Vibration and Active Control* 12.4, pp. 149–155. DOI: 10.1177/026309239301200404.

Kurokawa, A. K., H. Ishibashi, T. Miwa, and F. Nanayama (2018). "Rheological behavior of water-ash mixtures from Sakurajima and Ontake volcanoes: implications for lahar flow dynamics". *Bulletin of Volcanology* 80.6. DOI: 10.1007/s00445-018-1224-2.

Lai, V. H., V. C. Tsai, M. P. Lamb, T. P. Ulizio, and A. R. Beer (2018). "The Seismic Signature of Debris Flows: Flow Mechanics and Early Warning at Montecito, California". *Geophysical Research Letters* 45.11, pp. 5528–5535. DOI: 10.1029/2018gl077683.

Lavigne, F. and H. Suwa (2004). "Contrasts between debris flows, hyperconcentrated flows and stream flows at a channel of Mount Semeru, East Java, Indonesia". *Geomorphology* 61.1-2, pp. 41–58. DOI: 10.1016/j.geomorph.2003.11.005.

Lavigne, F. and J.-C. Thouret (2000). "Les lahars depots, origines et dynamique". *Bulletin de la Société Géologique de France* 171.5, pp. 545–557. DOI: 10.2113/171.5.545.

– (2003). "Sediment transportation and deposition by rain-triggered lahars at Merapi Volcano, Central Java, Indonesia". *Geomorphology* 49.1-2, pp. 45–69. DOI: 10.1016/s0169-555x(02)00160-5.

Lockwood, J. P. and R. W. Hazlett (2010). *Volcanoes: global perspectives*. John Wiley & Sons. ISBN: 978-1-4051-6249-4.

Lyons, J. J. and G. P. Waite (2011). "Dynamics of explosive volcanism at Fuego volcano imaged with very long period seismicity". *Journal of Geophysical Research* 116.B9. DOI: 10.1029/2011jb008521.

Lyons, J. J., G. P. Waite, W. I. Rose, and G. Chigna (2010). "Patterns in open vent, strombolian behavior at Fuego volcano, Guatemala, 2005–2007". *Bulletin of Volcanology* 72.1, pp. 1–15. DOI: 10.1007/s00445-009-0305-7.

Manville, V., K. A. Hodgson, B. F. Houghton, J. R. (Keys, and J. D. L. White (2000). "Tephra, snow and water: complex sedimentary responses at an active snow-capped stratovolcano, Ruapehu, New Zealand". *Bulletin of Volcanology* 62.4-5, pp. 278–293. DOI: 10.1007/s004450000096.

Manville, V., K. A. Hodgson, and J. D. L. White (1998). "Rheological properties of a remobilised-tephra lahar associated with the 1995 eruptions of Ruapehu volcano, New Zealand". *New Zealand Journal of Geology and Geophysics* 41.2, pp. 157–164. DOI: 10.1080/00288306.1998.9514800.

Marchetti, E., M. Ripepe, A. Harris, and D. Delle Donne (2009). "Tracing the differences between Vulcanian and Strombolian explosions using infrasonic and thermal radiation energy". *Earth and Planetary*

Science Letters 279.3-4, pp. 273–281. DOI: 10.1016/j.epsl.2009.01.004.

Marchetti, E., F. Walter, G. Barfucci, R. Genco, M. Wenner, M. Ripepe, B. McArdell, and C. Price (2019). "Infrasound Array Analysis of Debris Flow Activity and Implication for Early Warning". *Journal of Geophysical Research: Earth Surface* 124.2, pp. 567–587. DOI: 10.1029/2018jf004785.

Marcial, S., A. A. Melosantos, K. C. Hadley, R. G. LaHusen, and J. N. Marso (1996). "Instrumental lahar monitoring at Mount Pinatubo". *Fire and mud: Eruptions and lahars of Mount Pinatubo, Philippines*. Ed. by C. G. Newhall and R. Punongbayan. Philippine Institute of Volcanology, Seismology, and Seattle University, pp. 1015–1022.

Matthews, A. J. (2002). "Rainfall-induced volcanic activity on Montserrat". *Geophysical Research Letters* 29.13. DOI: 10.1029/2002gl014863.

Moretti, L., A. Mangeney, Y. Capdeville, E. Stutzmann, C. Huggel, D. Schneider, and F. Bouchut (2012). "Numerical modeling of the Mount Steller landslide flow history and of the generated long period seismic waves". *Geophysical Research Letters* 39.16, n/a–n/a. DOI: 10.1029/2012gl052511.

Naismith, A. K., I. M. Watson, R. Escobar-Wolf, G. Chigna, H. Thomas, D. Coppola, and C. Chun (2019). "Eruption frequency patterns through time for the current (1999–2018) activity cycle at Volcán de Fuego derived from remote sensing data: Evidence for an accelerating cycle of explosive paroxysms and potential implications of eruptive activity". *Journal of Volcanology and Geothermal Research* 371, pp. 206–219. DOI: 10.1016/j.jvolgeores.2019.01.001.

Ogiso, M. and K. Yomogida (2015). "Estimation of locations and migration of debris flows on Izu-Oshima Island, Japan, on 16 October 2013 by the distribution of high frequency seismic amplitudes". *Journal of Volcanology and Geothermal Research* 298, pp. 15–26. DOI: 10.1016/j.jvolgeores.2015.03.015.

Parfitt, L. and L. Wilson (2009). *Fundamentals of physical volcanology*. John Wiley & Sons. ISBN: 9781444307566.

Phillips, C. J. and T. R. Davies (1991). "Determining rheological parameters of debris flow material". *Geomorphology* 4.2, pp. 101–110. DOI: 10.1016/0169-555x(91)90022-3.

Pierson, T. C. (1985). "Initiation and flow behavior of the 1980 Pine Creek and Muddy River lahars, Mount St. Helens, Washington". *Geological Society of America Bulletin* 96.8, p. 1056. DOI: 10.1130/0016-7606(1985)96<1056:iafbot>2.0.co;2.

– (2005). "Hyperconcentrated flow — transitional process between water flow and debris flow". *Debris-flow Hazards and Related Phenomena*. Ed. by M. Jakob and O. Hungr. Springer Berlin Heidelberg, pp. 159–202. ISBN: 978-3-540-27129-1. DOI: 10.1007/3-540-27129-5_8.

Pierson, T. C. and J. E. Costa (1987). "A rheologic clasification of subaerial sediment-water flows". *Debris Flows/Avalanches: Process, Recognition, and Mitigation.* Geological Society of America, pp. 1–12. DOI: 10.1130/reg7-p1.

Pierson, T. C., R. J. Janda, J.-C. Thouret, and C. A. Borrero (1990). "Perturbation and melting of snow and ice by the 13 November 1985 eruption of Nevado del Ruiz, Colombia, and consequent mobilization, flow and deposition of lahars". *Journal of Volcanology and Geothermal Research* 41.1-4, pp. 17–66. DOI: 10.1016/0377-0273(90)90082-q.

Pierson, T. C. and J. J. Major (2014). "Hydrogeomorphic Effects of Explosive Volcanic Eruptions on Drainage Basins". *Annual Review of Earth and Planetary Sciences* 42.1, pp. 469–507. DOI: 10.1146/annurev-earth-060313-054913.

Pierson, T. C., J. J. Major, Á. Amigo, and H. Moreno (2013). "Acute sedimentation response to rainfall following the explosive phase of the 2008–2009 eruption of Chaitén volcano, Chile". *Bulletin of Volcanology* 75.5. DOI: 10.1007/s00445-013-0723-4.

Rickenmann, D., J. M. Turowski, B. Fritschi, A. Klaiber, and A. Ludwig (2012). "Bedload transport measurements at the Erlenbach stream with geophones and automated basket samplers". *Earth Surface Processes and Landforms* 37.9, pp. 1000–1011. DOI: 10.1002/esp.3225.

Ripepe, M., E. Marchetti, D. Delle Donne, R. Genco, L. Innocenti, G. Lacanna, and S. Valade (2018). "Infrasonic Early Warning System for Explosive Eruptions". *Journal of Geophysical Research: Solid Earth* 123.11, pp. 9570–9585. DOI: 10.1029/2018jb015561.

Ripepe, M., S. De Angelis, G. Lacanna, P. Poggi, C. Williams, E. Marchetti, D. D. Donne, and G. Ulivieri (2009). "Tracking Pyroclastic Flows at Soufrière Hills Volcano". *Eos, Transactions American Geophysical Union* 90.27, p. 229. DOI: 10.1029/2009eo270001.

Ronan, T. J., J. M. Lees, T. D. Mikesell, J. F. Anderson, and J. B. Johnson (2017). "Acoustic and Seismic Fields of Hydraulic Jumps at Varying Froude Numbers". *Geophysical Research Letters* 44.19, pp. 9734–9741. DOI: 10.1002/2017gl074511.

Schmandt, B., R. C. Aster, D. Scherler, V. C. Tsai, and K. Karlstrom (2013). "Multiple fluvial processes detected by riverside seismic and infrasound monitoring of a controlled flood in the Grand Canyon". *Geophysical Research Letters* 40.18, pp. 4858–4863. DOI: 10.1002/grl.50953.

Scott, K. M. (1988). *Origins, behavior, and sedimentology of lahars and lahar-runout flows in the Toutle-Cowlitz River system.* Professional Paper 1447-A.

Sukatja, C. B. (2016). "Early Warning System for Lahar Flow Based on Lahar Arrival Time Forecasting". *Journal of Applied Environmental and Biological Sciences* 6.11, pp. 11–21.

Suwa, H., K. Okano, and T. Kanno (2011). "Forty years of debris-flow monitoring at Kamikamihorizawa Creek, Mount Yakedake, Japan". *Italian Journal of Engineering Geology and Environment* 201103, pp. 605–613. DOI: 10.4408/IJEGE.2011-03.B-066.

Swanson, F. J. and J. J. Major (2005). "Physical Events, Environments, and Geological—Ecological Interactions at Mount St. Helens: March 1980–2004". *Ecological Responses to the 1980 Eruption of Mount St. Helens.* Ed. by D. V. H., S. F. J., and C. C.M. Springer, New York, NY., pp. 27–44. DOI: 10.1007/0-387-28150-9_3.

Thouret, J.-C., K. E. Abdurachman, J.-L. Bourdier, and S. Bronto (1998). "Origin, characteristics, and behaviour of lahars following the 1990 eruption of Kelud volcano, eastern Java (Indonesia)". *Bulletin of Volcanology* 59.7, pp. 460–480. DOI: 10.1007/s004450050204.

Thouret, J.-C., S. Antoine, C. Magill, and C. Ollier (2020). "Lahars and debris flows: Characteristics and impacts". *Earth-Science Reviews* 201, p. 103003. DOI: 10.1016/j.earscirev.2019.103003.

Vallance, J. W., S. P. Schilling, O. Matías, W. I. Rose, and M. M. Howell (2001). *Volcano hazards at Fuego and Acatenango, Guatemala.* DOI: 10.3133/ofr01431. Open-File Report 2001-431.

Vallance, J. W. and R. M. Iverson (2015). "Lahars and Their Deposits". *The Encyclopedia of Volcanoes.* Ed. by H. Sigurdsson. Elsevier, pp. 649–664. DOI: 10.1016/b978-0-12-385938-9.00037-7.

Walsh, B., V. Coviello, L. Capra, J. Procter, and V. Márquez-Ramirez (2020). "Insights Into the Internal Dynamics of Natural Lahars From Analysis of 3-Component Broadband Seismic Signals at Volcán de Colima, Mexico". *Frontiers in Earth Science* 8. DOI: 10.3389/feart.2020.542116.

Zanuttigh, B. and A. Lamberti (2007). "Instability and surge development in debris flows". *Reviews of Geophysics* 45.3. DOI: 10.1029/2005rg000175.

Zobin, V. M., I. Plascencia, G. Reyes, and C. Navarro (2009). "The characteristics of seismic signals produced by lahars and pyroclastic flows: Volcán de Colima, México". *Journal of Volcanology and Geothermal Research* 179.1-2, pp. 157–167. DOI: 10.1016/j.jvolgeores.2008.11.001.